

Flow distortion recorded by sonic anemometers on a long-span bridge: towards a better modelling of the dynamic wind load in full-scale.

Etienne Cheynet^{a,*}, Jasna Bogunović Jakobsen^a, Jonas Snæbjörnsson^{a,b}

^a*Department of Mechanical and Structural Engineering and Materials Science, University of Stavanger, N-4036 Stavanger, Norway*

^b*School of Science and Engineering, Reykjavík University, Menntavegur 1, 101 Reykjavík, Iceland*

Abstract

The turbulent wind field around a suspension bridge deck is studied using eleven months of full-scale records from sonic anemometers mounted above the girder. Using the mean and turbulent velocity characteristics, we demonstrate that the bridge structure can significantly distort the flow. More precisely, the friction velocity, the variance of the fluctuating vertical velocity and the mean wind incidence angle are underestimated on the downstream side of the deck. The terrain is also found to influence the flow in a non-negligible way, such that turbulence characteristics differ significantly from those observed in flat and homogeneous terrains. For a hexagonal girder with a width to height ratio $B/H \approx 4.5$, deck-induced flow distortion is still observed on the downwind side of the girder at a height above the road equal to $3.6H$. This further supports the idea that wind measurements from a suspension bridge should rely on anemometers on both sides of the deck to mitigate flow distortion. The improved flow description combined with high-resolution acceleration records of the deck provides a simulation of the wind-induced response of the bridge with a level of accuracy that is rarely achieved in full-scale. In particular, the limits of a wind model based on flat terrain assumption as well as the limits of the strip theory are highlighted by the recorded data and the improved modelling of the bridge buffeting response.

Keywords: Full-scale, Flow distortion, Sonic anemometer, Buffeting theory, Suspension bridge, Complex terrain

1. Introduction

Measurements of wind turbulence above the deck of long-span cable-suspended bridges in full-scale can be traced back to the 1970s [1, 2]. The data gathered this way can be used to model the dynamic wind load acting on the deck [3–8], as well as to conveniently study the horizontal structure of atmospheric turbulence without deploying multiple met-masts. However, the possible flow distortion caused by the bridge deck has rarely been studied in details. Jensen and Hjort-Hansen [1] noted for the case of the Sotra suspension bridge (Norway), which has a truss girder, that the anemometer records collected 3 m above the upwind side of the deck were influenced by the bridge structure. This influence was, however, assumed small enough to be neglected. They found an average incidence angle of 7° and

*Corresponding author

Email address: etienne.cheynet@uis.no (Etienne Cheynet)

9 the turbulence statistics were thus studied in the streamline coordinate system, i.e. in a coordinate system where the
10 vertical mean wind speed is as close as possible to 0 m s^{-1} . Hay [3, 9] estimated the power spectral density (PSD) of the
11 along-wind and vertical velocity components at two positions above the Erskine Bridge (UK), which has a 31 m-wide
12 and 3.2 m-high trapezoidal deck. The first position was on a 7 m-high boom on the upwind side of the deck, whereas
13 the second one was on a 9 m-high lamp standard near the middle part of the deck, widthwise. For the latter sensor, Hay
14 [3] found that the vertical velocity spectrum was clearly distorted, whereas the along-velocity spectrum was much less
15 affected by the presence of the girder. Frandsen [10] used finite element flow simulations to access the expected flow
16 disturbances by the Great Belt East suspension bridge deck. The analysis, considering the deck without the railings,
17 indicated that the cup anemometer installed 2.3 m above the upwind side of the deck was expected to be located in the
18 undisturbed mean free-stream velocity region. On the downwind side, a height of 2 m was considered sufficient.

19 The aforementioned observations underline the complex influence of the deck geometry on the flow measured by
20 anemometers. They also reflect the need for improved understanding of flow distortion by a bridge deck in full-scale
21 for a better modelling of the wind forces acting on the structure. Since 2013, the Lysefjord suspension bridge (Norway)
22 has been used as a full-scale laboratory to study the wind effects on a long-span bridge in complex terrain [11]. Since
23 July 2017, the flow has been recorded by 9 sonic anemometers installed on both the upwind and downwind side of
24 the girder, whereas four pairs of accelerometers monitor the deck vibrations. Using eleven months of atmospheric
25 measurement and full-scale acceleration records, from July 2017 through May 2018, we investigate the bridge girder
26 influence on the flow across the deck and the associated wind-induced response.

27 Flow distortion is here defined as the deviation of wind velocity characteristics from those estimated in flat and
28 homogeneous terrain with an infinite fetch. Therefore, we distinguish between girder induced flow distortion and
29 terrain-induced flow distortion, often referred to as “orography” effects. An additional distortion of the recorded
30 turbulence signal originates in the interaction between anemometer geometry and the flow through the sensor head.
31 This “sensor-induced flow distortion” refers to both the shadowing effect of the transducer and the flow interruption
32 of the frame of the anemometer. The sensor induced flow distortion leads to an angle of attack error that is usually
33 reduced using an appropriate calibration [12] but that can still be non-negligible under highly turbulent conditions [13].

34 The present paper is organized as follows: In section 2, the bridge instrumentation and the data post-processing
35 are presented. Section 3 compares the turbulence characteristics estimated using the sonic anemometers on both the
36 upwind and downwind side of the girder. Section 4 assesses how the sonic anemometer position affects the computed
37 bridge response and discusses the limits of the strip assumption from a full-scale perspective.

38 **2. Instrumentation and methods**

39 *2.1. Bridge instrumentation*

40 The Lysefjord bridge is a suspension bridge with a main span of 446 m, crossing the inlet of a narrow and long fjord
41 with an azimuth of -42° (fig. 1). The fjord is enclosed by mountains and steep hills that channel the flow, such that two

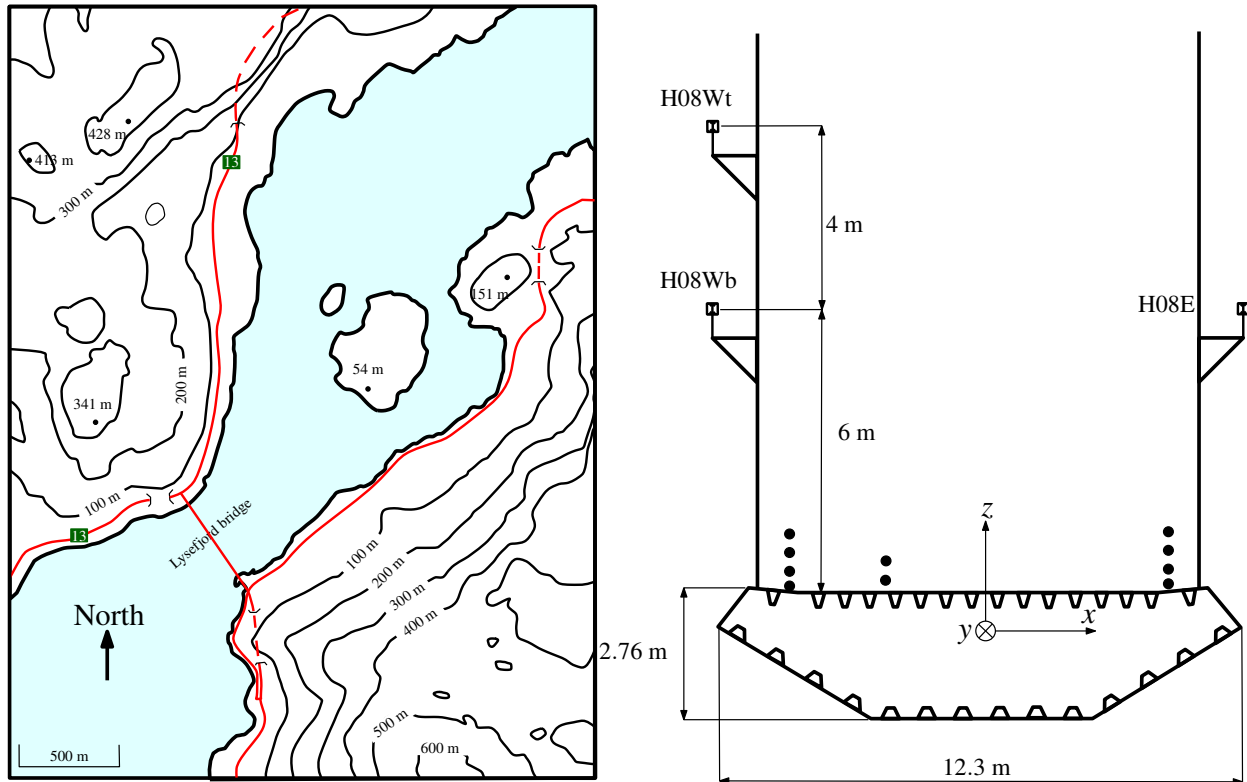


Figure 1: Left: topographic map of the Lysefjord bridge. Right: sketch of the cross-section of the Lysefjord bridge deck on hanger 08.

42 main wind directions are primarily observed. The first sector corresponds to a flow from north-northeast, i.e. from the
 43 inside of the fjord, at azimuth between 0° and 60° . The second one corresponds to a flow from south-southwest, i.e. a
 44 wind direction between 180° and 270° .

45 The Lysefjord bridge has been instrumented with a wind and structural monitoring system since November 2013
 46 [11]. In June 2017, the arrangement of the wind sensors was modified and three sonic anemometers were installed on
 47 the east side of the bridge. In fig. 2, the position of the anemometers above the deck is defined using the hanger name
 48 HXY, where X is a digit between 08 and 24 indicating the hanger number, and Y denotes the west side (W) or east side
 49 (E) of the deck. Since two anemometers are mounted on the west hanger no. 08 (H08W), the notations H08Wb and
 50 H08Wt refer to the sonic anemometer mounted 6 m (bottom) and 10 m (top) above the deck, respectively. Eight of
 51 the sonic anemometers are 3-D WindMaster Pro from Gill instruments (Lymington, UK), which can operate with a
 52 sampling frequency up to 32 Hz. The last sonic anemometer, mounted on H10W, is a Weather Transmitter WXT520
 53 from Vaisala (Helsinki, Finland), which monitors the horizontal wind components, rainfall, relative humidity, pressure
 54 and absolute temperature with a sampling frequency up to 4 Hz.

55 Four pairs of tri-axial accelerometers (CUSP-3D from Canterbury Seismic Instruments) are installed inside the
 56 deck near hangers H-09, H-18, H-24 and H-30. Each pair can operate with a sampling frequency up to 200 Hz and is
 57 mounted on both sides of the deck so that the vertical and torsional bridge responses can be studied separately. The

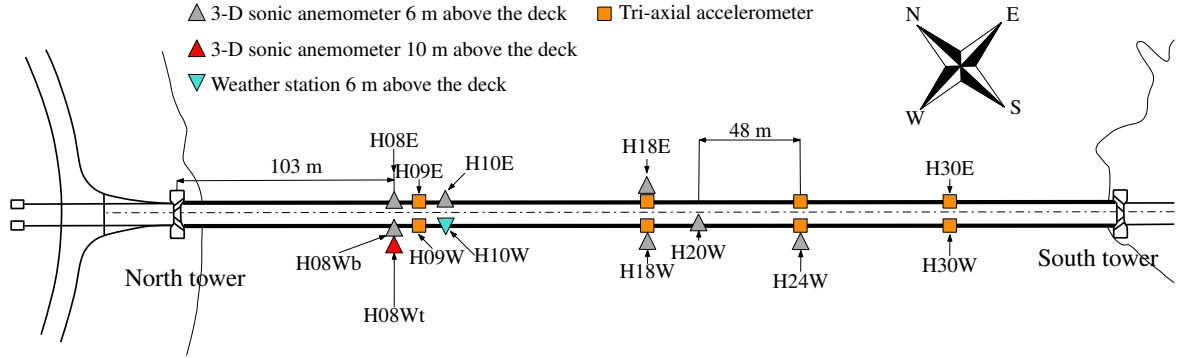


Figure 2: Instrumentation of the Lysefjord bridge since June 2017. The distance between each hanger is 12 m.

58 data are recorded in groups, by five acquisition units. A master data logging unit synchronizes all the data into a single
 59 data file, which is then continuously transmitted via a mobile net.

60 2.2. Data processing

61 The along-wind, crosswind and vertical wind velocity components are denoted u , v and w (positive z -axis),
 62 respectively. Each component is expressed as the sum of a mean component, denoted by an overbar, and a fluctuating
 63 component with zero mean denoted by a prime, defined as a Gaussian stationary random process, such that for
 64 $j = \{u, v, w\}$, one can write $j = \bar{j} + j'$.

65 The sonic anemometers deployed on the Lysefjord bridge continuously monitor the flow and the amount of data
 66 gathered is, therefore, enormous. The data post-processing is done as follows:

- 67 (a) time series are de-spiked and decimated down to a frequency of 25 Hz to facilitate data handling.
- 68 (b) Unphysical signals characterized by an absolute value of the skewness above 2 or a kurtosis above 8 are dismissed
 69 [14, 15].
- 70 (c) The underestimation of the vertical wind velocity component due to angle of attack errors [13] is corrected
 71 during the post-processing of the data using the correction provided by Gill Instrument, which is a multiplication
 72 scaling factor. Note that the anemometers located on H08E and H10E, are new, from an updated production lot,
 73 and do not need such a correction.
- 74 (d) The coordinate system is rotated such that $\bar{v} \approx \bar{w} \approx 0$. The study in such a coordinate system can be done using
 75 the planar-fit (PF) algorithm [16, 17], the double rotation method or triple rotation method [18]. In the present
 76 case, the high complexity of the terrain justifies the application of the double rotation technique rather than a
 77 sectoral PF algorithm, which may have a limited applicability in such an environment [19].
- 78 (e) Non-stationary samples are omitted in the further analysis as well as those associated with a mean wind speed
 79 below 6 m s^{-1} . Only the second-order stationarity is considered here, i.e. the time-dependency of statistical

80 moments up to order two. For each time series, the centred moving mean and moving standard deviation are
 81 studied, using a half window length of 5 min. If a local deviation from the mean or standard deviation greater
 82 than 40 % is detected, the time series is assumed non-stationary and dismissed. The values of the threshold
 83 parameters and window length have been chosen using simulated stationary turbulent wind velocity histories
 84 that are generated using the method by Shinozuka and Deodatis [20], which showed that such a choice was
 85 appropriate to differentiate between the random error, due to the finite averaging time, and the error due to
 86 non-stationary fluctuations.

- 87 (f) Following Stiperski and Rotach [15], the measurement uncertainties in the variance and covariance of the wind
 88 velocity records are assessed. For the wind velocity component $j = \{u, v, w\}$, the measurement uncertainty a_j for
 89 the variance is defined as,

$$a_{jj}^2 = \frac{4z}{\tau \bar{u}(z)} [\kappa_j - 1] \quad (1)$$

90 where τ is the averaging time; κ_j is the kurtosis of the velocity component j and $\bar{u}(z)$ is the mean wind speed at a
 91 height z above the ground. Similarly, the measurement uncertainty for the covariance $\overline{u'w'}$ and $\overline{v'w'}$ between the
 92 horizontal wind components and the vertical wind component are defined as:

$$a_{uw}^2 = \frac{z}{\tau \bar{u}(z)} \left[\frac{(\overline{u'w'})^2}{u_*^4} - 1 \right] \quad (2)$$

$$a_{vw}^2 = \frac{z}{\tau \bar{u}(z)} \left[\frac{(\overline{v'w'})^2}{u_*^4} - 1 \right] \quad (3)$$

93 where u_* is the friction velocity, calculated as advised by Weber [21]:

$$u_* = \left(\overline{u'w'^2} + \overline{v'w'^2} \right)^{1/4} \quad (4)$$

94 As eqs. (1) to (3) show, the measurement uncertainty is affected by the time series duration. Longer time series
 95 should reduce the measurement uncertainties but also increase the number of non-stationary records, thereby
 96 reducing the amount of suitable data for the analysis. Therefore, a duration of 30 min was found better suited to
 97 collect a larger number of high-quality data. For that averaging time, the median value of a_{ii} , where $i, j = \{u, v, w\}$,
 98 is ca. 20 % whereas the median value for a_{uw} and a_{vw} is around 33 %. Samples associated with a measurement
 99 uncertainty above 50 % are disregarded as advised by Stiperski and Rotach [15], which accounts for ca. 8 % of
 100 samples with a mean wind speed above 6 m s^{-1} .

- 101 (g) Turbulence characteristics are studied after removing the mean and any linear trend from the approved time
 102 series.

103 The atmospheric stability is estimated using the non-dimensional Obukhov length ζ , local scaling [22, 23] and
 104 assuming that the virtual potential temperature is well approximated by the sonic temperature:

$$\zeta = \frac{-g\kappa z \overline{w'\theta'_v}}{\overline{\theta}_v u_*^3} \quad (5)$$

105 where $g = 9.81 \text{ m s}^{-2}$ is the acceleration of gravity; $\overline{\theta}_v$ is the average virtual potential temperature; $\overline{w'\theta'_v}$ is the flux of
 106 virtual potential temperature and $\kappa \approx 0.4$ is the von Kármán constant. Only samples characterized by $|\zeta| < 0.1$, which
 107 represents near-neutral conditions, are considered in the following.

108 The one-point power-spectral density (PSD) estimates of the velocity fluctuations are denoted S_j , where $j =$
 109 $\{u, v, w\}$, and are computed using the periodogram method with a Hamming window. The periodogram method is
 110 generally associated with a large random error, which is reduced by block-averaging each individual spectra into 60 bins
 111 equally spaced on a logarithmic scale. Then, each PSD estimate is normalized and ensemble averaged. As the record
 112 duration is 30 min, the lowest frequency recorded is 0.56 mHz. The real part of the normalized cross-spectrum, called
 113 co-coherence, is estimated using Welch's algorithm [24] with a Hamming window, six segments and 50 % overlapping.

114 In addition to the one-point velocity spectra and cross-spectra, the turbulence intensity I_j , where $j = \{u, v, w\}$, is
 115 studied at wind velocities large enough so that I_j produce stable values. We recall that I_j is defined as

$$I_j(z) = \frac{\sigma_j(z)}{\overline{u}(z)} \quad (6)$$

116 where σ_j is the standard deviation of the velocity component j .

117 2.3. Wind load and bridge response modelling

118 The action of atmospheric turbulence on a wind-sensitive structure is named buffeting load and the associated
 119 dynamic response is named buffeting response [25, 26]. The frequency domain approach, which relies on the
 120 computation of the power spectral density and the associated standard deviation of the bridge displacement and/or
 121 vertical response is considered in the following.

122 In the present study, only the vertical bridge acceleration response is computed, which for simplicity is evaluated
 123 using the vertical wind velocity component only. This relies on the assumption that the fluctuating horizontal velocity
 124 components have a negligible influence on the dynamic vertical bridge response, which is generally verified for the
 125 wind conditions recorded on the Lysefjord bridge site [27, p. 146]. The buffeting response of the Lysefjord bridge is
 126 computed using the quasi-steady assumption, i.e. assuming that the flow instantaneously adapts to the moving bridge
 127 deck such that the aerodynamic coefficients and their first derivative are independent of the frequency. The aerodynamic
 128 forces are linearised with respect to the time-dependent angle of attack, using Taylor series up to order 1. As shown in
 129 Cheynet et al. [28], the linearisation of the buffeting load is justified for the study of the vertical bridge response, even
 130 under highly turbulent conditions. Modal coupling effects are neglected as the wind velocities studied are not high

131 enough to generate significant coupling effects. Finally, the strip assumption is used, i.e. the correlation of the wind
 132 forces along and across the bridge deck is taken to be identical to that of the undisturbed, incoming wind fluctuations,
 133 implying that the cross-sectional aerodynamic admittance is equal to one at every frequency.

134 If the flow is not perpendicular to the bridge longitudinal axis, it is said “skewed” and the angle between the normal
 135 to the deck and the wind direction is the “yaw angle” β . The horizontal wind velocity component normal to the deck is
 136 here denoted v_x ,

$$v_x = u \cos(\beta) + v \sin(\beta) \quad (7)$$

137 The dynamic wind-induced response of the bridge deck in the vertical direction is dominated by the vertical wind
 138 velocity component, so that the spectral wind load can be written as:

$$S_q(y_i, y_j, f) = \left[\frac{1}{2} \rho \bar{v}_x B \left(C'_L + \frac{H}{B} C_D \right) \right]^2 \sqrt{S_w(y_i, f) \cdot S_w(y_j, f) \cdot \gamma_w(y_i, y_j, f)} \quad (8)$$

139 where \bar{v}_x is the horizontal mean wind velocity component normal to the span; $B = 12.3$ m and $H = 2.76$ m are the
 140 girder width and height, respectively; $C'_L = 3.0$ is the first derivative of the lift coefficient with respect to the incidence
 141 angle; $C_D = 1.0$ is the drag coefficient; $S_w(y_i, f)$ is the vertical velocity spectrum at the coordinate y_i and $\gamma_w(y_i, y_j, f)$ is
 142 the along-span co-coherence of the vertical velocity component between the coordinates y_i and y_j . As pointed out by
 143 Xie et al. [29], the coherence of turbulence γ_w is also affected by the yaw angle. In the present case, the yaw angle is
 144 accounted for in the expression of γ_w using the along-span separation instead of the crosswind separation, as done
 145 previously by e.g. Saranyasoontorn et al. [30].

146 The spectrum of the modal wind load S_Q is associated with the mode shapes $\Phi(y)$ of the bridge deck, on which the
 147 buffeting load is concentrated,

$$S_Q(f) = \int_0^L \int_0^L \Phi(y_i) S_q(y_i, y_j, f) \Phi(y_j) dy_i dy_j \quad (9)$$

148 The power spectral density of the bridge response is

$$S_{r_z}(y, f) = [\Phi(y) \cdot \mathbf{H}(f)] \cdot S_Q(f) \cdot [\Phi(y) \cdot \mathbf{H}(f)]^T, \quad (10)$$

149 where $\mathbf{H}(f)$ is the mechanical admittance of the system modified by the modal aerodynamic damping and stiffness.
 150 The mode shapes $\Phi(y)$ and eigenfrequencies of the Lysefjord bridge are computed using a continuum bridge model and
 151 the Galerkin method [31, 32]. The modal parameters have been validated and/or corrected using an operational modal
 152 analysis relying on an automated covariance-driven stochastic subspace identification algorithm [28, 33].

153 The standard deviation of the computed bridge displacement response is denoted $\sigma_{r_z}(y)$ and is computed as

$$\sigma_{r_z}(y) = \sqrt{\int_0^{\infty} S_{r_z}(y, f) df}. \quad (11)$$

154 The vertical turbulent wind load is modelled using the one-point spectra and coherence estimated at mid-span.

155 Generally a single spectral model is desired to describe the velocity spectra on both sides of the deck. However, as
156 the spectra affected by flow distortion may have a flattened spectral peak the following spectral form is adopted:

$$\frac{fS_w(f)}{\sigma_i^2} = \frac{a_1 f_r}{(1 + b_1 f_r)^{5/3}} + \frac{a_2 f_r}{1 + b_2 f_r^{5/3}} \quad (12)$$

157 where a_1 , a_2 , b_1 and b_2 are parameters to be determined and f_r is the reduced frequency defined as

$$f_r = \frac{fz}{\bar{u}} \quad (13)$$

158 For a flow perpendicular to the bridge deck, the co-coherence γ_w is often modelled using the Davenport model [34]:

$$\gamma_w(y_i, y_j, f) \approx \exp(-Cf|y_j - y_i|/\bar{u}(z)), \quad (14)$$

159 where y_i and y_j are two measurement positions; C is a constant named ‘‘decay coefficient’’ and f is the frequency.

160 However, we model here γ_w as a three-parameter exponential decay function:

$$\gamma_w(y_i, y_j, f) = \exp\left\{-\left[\frac{|y_j - y_i|}{\bar{u}} \sqrt{(c_1 f)^2 + c_2^2}\right]\right\} \cos\left(c_3 \frac{|y_j - y_i| f}{\bar{u}}\right) \quad (15)$$

161 where c_1 , c_2 and c_3 are three decay parameters permitting the co-coherence to be negative and to have a realistic
162 behaviour at large spatial separations, for which the maximum value of γ_w becomes lower than unity at zero frequency.

163 For a given mean wind speed and frequency, the co-coherence is assumed here to be a function of the spatial separation
164 $d_y = |y_i - y_j|$ only, such that $\gamma_w(d_y, f) \approx \gamma_w(y_i, y_j, f)$. If the flow is not perpendicular to the bridge longitudinal axis, the
165 crosswind separation is replaced by the along-span separation:

$$\gamma_w(d_y, f) = \exp\left\{-\left[\frac{d_y \cos(\beta)}{\bar{u}} \sqrt{(c_1 f)^2 + c_2^2}\right]\right\} \cos\left(c_3 \frac{d_y \cos(\beta) f}{\bar{u}}\right) \quad (16)$$

166 Although the approach adopted above to compute the bridge response is much simpler than in Cheynet et al. [28],
167 it provides a good illustration of the sensitivity of the bridge response to the vertical wind velocity component. In
168 the present study, only wind-induced vibrations are of interest and bridge acceleration records dominated by traffic

loading have, therefore, been dismissed. This is achieved by comparing the variance of the low-frequency part of the acceleration spectrum, arbitrarily defined as the range below 1 Hz, with the one from the high-frequency range [27, p. 186-189]. Acceleration samples with a dominant contribution from the high-frequency range are considered to be dominated by traffic-induced vibrations and thus disregarded. Similarly, the possible flow distortion induced by vehicles is assumed negligible in the current study. This is justifiable as the traffic flow rate is generally rather low on the bridge, especially in the cases when wind-induced vibrations are the dominant source of excitation.

3. Results

Figure 3 displays the mean wind speed and the along-wind turbulence intensity estimated on the Lysefjord bridge from July 2017 to May 2018. The high turbulence intensity recorded, previously mentioned in Cheynet et al. [28], is consistent with measurements from other Norwegian fjords [35]. It suggests that buoyancy-generated turbulence effects are not dominant in the flow. For the period considered, this is also indicated by the stability parameter ζ , for which 61 % of the values are bounded between -0.1 and 0.1 . The different sonic anemometers give values of ζ that are similar on average, but those corrected for the underestimation of the vertical wind velocity component provide estimates with a considerable scatter, leading to a significant reduction of the data availability. For this reason, the value of ζ used to select samples associated with near-neutral conditions, is estimated from the sonic anemometer on H10E only.

Whereas the flow from north-northeast is generally more turbulent than the one from south-southwest, the largest velocities are recorded for the latter sector. Nevertheless, the flow from south-southwest is associated with a turbulence intensity above 0.20 when the wind direction is between 180° and 190° , for which the flow brushes past the west face of the mountain on the south side of the bridge.

3.1. Mean flow characteristics

A relative difference between the mean wind speed estimated from a reference sonic anemometer and the others, denoted ϵ_u , is investigated in Table 1. The reference sensor is the one located on H18W or H18E for a wind from south-southwest or north-northeast, respectively. Note that the discrepancies due to slightly different measurement heights are not corrected for as the wind shear difference is assumed small. It should also be noted that the anemometer on H10W does not measure the vertical component and, therefore, cannot provide any indication of the wind incidence angle.

For a flow from south-southwest, Table 1 shows that, on average, the absolute relative difference is lower than 4 %, indicating that for this particular wind sector the deck has limited influence on the mean flow on the downwind side of the bridge. The larger discrepancies observed between the mean speed measurements on H18W and H24W may be due to terrain-induced flow inhomogeneity. This was previously suggested in Cheynet et al. [36], where lidar measurements indicated the existence of a non-uniform mean flow on the south side of the bridge.

For a flow from north-northeast, the relative difference ϵ_u indicates a stronger flow inhomogeneity than for a flow from south-southwest. Values of ϵ_u larger than 8 % on H08Wb and H08Wt cannot be simply due to the influence of the

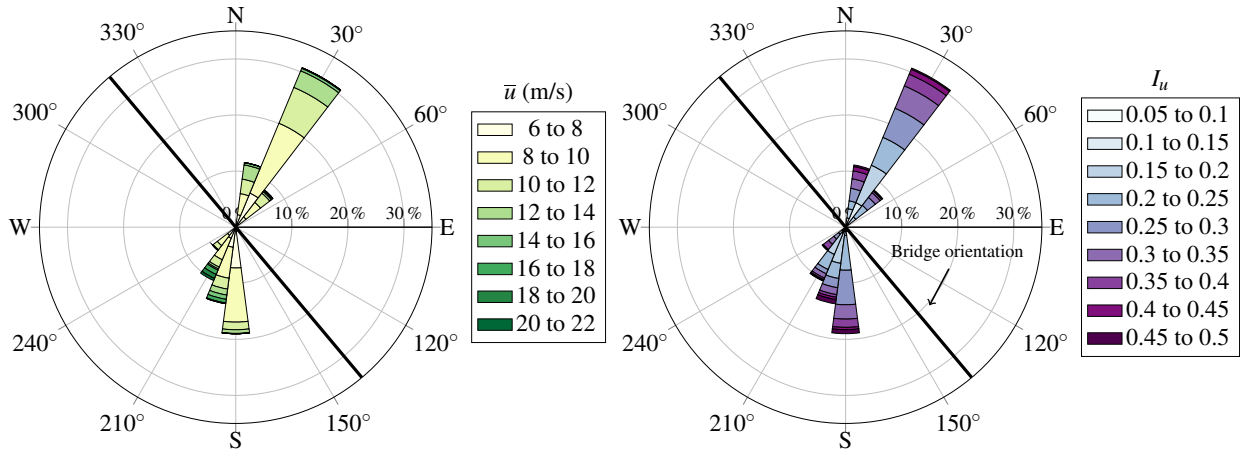


Figure 3: Mean wind speed (left) and along-wind turbulence intensity (right) recorded from every anemometer the Lysefjord bridge between July 2017 and May 2018 (1.7×10^3 stationary records of 30 min duration with $\bar{u} \geq 6 \text{ m s}^{-1}$).

Table 1: Average relative percentage wise difference ϵ_u in the recorded mean wind speed and mean incidence angle α along the deck of the Lysefjord bridge for samples with $\bar{u} \geq 6 \text{ m s}^{-1}$ and a 30 min averaging time (865 samples for a flow NNE and 697 samples for a flow from SSW).

Sensors		Wind Direction			
West side	East side	south-southwest		north-northeast	
		ϵ_u (%)	$\bar{\alpha}$ ($^\circ$)	ϵ_u (%)	$\bar{\alpha}$ ($^\circ$)
H08Wb	-	-0.7	3.5	11.0	-0.4
H08Wt	-	-0.1	2.9	8.5	-1.1
H10W	-	-1.5	-	12.0	-
H18W	-	0	2.9	2.3	0.1
H20W	-	0.2	1.8	0.5	0.5
H24W	-	-2.4	0.5	-3.4	0.1
-	H08E	1.5	1.2	4.1	0.5
-	H10E	1.0	0.5	2.2	0.8
-	H18E	3.5	0.8	0	3.0

202 terrain on the flow. Different flow characteristics from the two wind sectors identified may, however, be responsible for
 203 different levels of flow distortion by the bridge deck.

204 The mean wind incidence angle $\bar{\alpha}$ recorded for the two wind sectors considered are displayed in Table 1 for
 205 $\bar{u} \geq 6 \text{ m s}^{-1}$. Whereas the south-southwest flow is characterized by $\bar{\alpha} \geq 3^\circ$ on average on the upwind side, which is
 206 non-negligible, the sensors located on the downwind side of the deck monitor a lower incidence angle, reflecting a
 207 possible influence of the bridge girder on the vertical mean speed recorded 6 m above the road. If a sonic anemometer is
 208 not perfectly levelled, a non-zero mean incidence angle is measured. For several anemometers monitoring a horizontal
 209 flow, this can lead to incidence angles that have various values if the levelling is slightly different for each sensor. For a

Table 2: Turbulence characteristics estimated from every sonic anemometer on the Lysefjord bridge, under near-neutral conditions, $\bar{u} > 10 \text{ m s}^{-1}$ for a wind from south-southwest (SSW) with 88 samples and north-northeast (NNE) with 166 samples.

Sector	Sensor location		$\frac{\sigma_w}{u_*}$	$\frac{\sigma_v}{u_*}$	$\frac{\sigma_u}{u_*}$	$\frac{\sigma_w}{\sigma_u}$	$\frac{\sigma_v}{\sigma_u}$
	West side	East side					
SSW	H08Wb	-	1.82 ± 0.55	2.83 ± 1.20	2.68 ± 0.73	0.71 ± 0.09	1.09 ± 0.22
	H08Wt	-	1.61 ± 0.30	2.47 ± 0.63	2.39 ± 0.41	0.68 ± 0.08	1.05 ± 0.22
	H10W	-	-	-	-	-	1.04 ± 0.17
	H18W	-	1.85 ± 1.10	2.95 ± 2.00	2.70 ± 1.30	0.69 ± 0.08	1.05 ± 0.23
	H20W	-	1.80 ± 0.56	2.83 ± 1.10	2.61 ± 0.71	0.69 ± 0.07	1.02 ± 0.21
	H24W	-	1.77 ± 0.51	3.01 ± 1.10	2.59 ± 0.65	0.70 ± 0.08	1.07 ± 0.26
	-	H08E	1.46 ± 0.23	2.83 ± 0.61	3.16 ± 0.62	0.49 ± 0.06	0.95 ± 0.17
	-	H10E	1.45 ± 0.20	3.02 ± 0.61	3.11 ± 0.46	0.48 ± 0.05	1.02 ± 0.16
	-	H18E	1.40 ± 0.17	3.00 ± 0.37	3.15 ± 0.49	0.46 ± 0.04	0.98 ± 0.19
NNE	H08Wb	-	1.42 ± 0.37	2.32 ± 0.69	2.91 ± 0.85	0.48 ± 0.04	0.79 ± 0.08
	H08Wt	-	1.52 ± 0.38	2.14 ± 0.59	2.64 ± 0.74	0.56 ± 0.05	0.79 ± 0.08
	H10W	-	-	-	-	-	0.78 ± 0.09
	H18W	-	1.65 ± 0.67	2.93 ± 1.20	3.53 ± 1.50	0.48 ± 0.04	0.86 ± 0.09
	H20W	-	1.75 ± 0.60	2.88 ± 1.10	3.44 ± 1.20	0.50 ± 0.05	0.85 ± 0.09
	H24W	-	1.60 ± 0.58	2.87 ± 1.00	3.45 ± 1.30	0.45 ± 0.05	0.80 ± 0.08
	-	H08E	1.39 ± 0.30	1.72 ± 0.44	2.05 ± 0.43	0.68 ± 0.06	0.84 ± 0.09
	-	H10E	1.42 ± 0.27	1.76 ± 0.39	2.03 ± 0.39	0.69 ± 0.06	0.86 ± 0.09
	-	H18E	1.53 ± 0.25	1.88 ± 0.33	2.28 ± 0.38	0.67 ± 0.06	0.83 ± 0.08

210 flow from north-northeast, which is more horizontal, such levelling imperfections may explain the more heterogeneous
211 values of the incidence angle recorded along the bridge deck. In summary, the study of the mean flow characteristics on
212 both sides of the deck indicates that the vertical mean wind velocity component may be slightly affected by the deck
213 whereas it is not the case for the along-wind component.

214 3.2. One-point turbulence characteristics

215 To study integrated turbulence characteristics on the bridge site in a consistent manner, it is important that the
216 turbulence intensity is more or less constant with the mean wind speed and the wind sector selected. As the turbulence
217 intensity was seen to stabilize as the mean wind approached 10 m s^{-1} , it was decided to consider only samples
218 characterized by $\bar{u} \geq 10 \text{ m s}^{-1}$ in the present subsection, although it reduces considerably the number of samples
219 available.

220 The estimated one-point turbulence characteristics are displayed separately for a wind direction from south-
221 southwest and north-northeast in Tables 2 and 3. The notation $y \pm x$, used in the following, indicates that x is the

Table 3: Same as Table 2, but for the turbulence intensity “as seen” by each sensor.

Sector	Sensor location		I_u	I_v	I_w
	West side	East side			
SSW	H08Wb	-	0.14 ± 0.05	0.16 ± 0.16	0.10 ± 0.03
	H08Wt	-	0.15 ± 0.05	0.16 ± 0.16	0.10 ± 0.03
	H10W	-	0.15 ± 0.05	0.16 ± 0.16	-
	H18W	-	0.15 ± 0.05	0.17 ± 0.17	0.11 ± 0.03
	H20W	-	0.16 ± 0.05	0.17 ± 0.17	0.11 ± 0.03
	H24W	-	0.16 ± 0.05	0.18 ± 0.18	0.11 ± 0.03
	-	H08E	0.16 ± 0.05	0.16 ± 0.16	0.08 ± 0.02
	-	H10E	0.15 ± 0.05	0.16 ± 0.16	0.07 ± 0.02
	-	H18E	0.17 ± 0.04	0.16 ± 0.16	0.08 ± 0.02
NNE	H08Wb	-	0.23 ± 0.07	0.18 ± 0.18	0.11 ± 0.03
	H08Wt	-	0.22 ± 0.07	0.18 ± 0.18	0.13 ± 0.04
	H10W	-	0.25 ± 0.06	0.20 ± 0.20	-
	H18W	-	0.23 ± 0.08	0.19 ± 0.19	0.11 ± 0.03
	H20W	-	0.23 ± 0.08	0.18 ± 0.18	0.12 ± 0.04
	H24W	-	0.22 ± 0.08	0.17 ± 0.17	0.10 ± 0.03
	-	H08E	0.24 ± 0.07	0.20 ± 0.20	0.17 ± 0.05
	-	H10E	0.23 ± 0.07	0.21 ± 0.21	0.17 ± 0.05
	-	H18E	0.24 ± 0.07	0.20 ± 0.20	0.17 ± 0.05

222 standard deviation associated with the ensemble-averaged quantity y . These tables show that the discrepancies observed
 223 between the upwind and downwind side are particularly important for the w component whereas they are not clearly
 224 defined for the horizontal components.

225 For a south-southwest flow, the ratio σ_w/u_* is slightly lower on the downwind side than on the upwind side, which
 226 must be interpreted with caution as the value generally found in the literature in flat terrain ranges from 1.2 to 1.3 [37],
 227 whereas it corresponds here to a flow likely distorted by the presence of the deck. Jensen and Hjort-Hansen [1] found a
 228 ratio σ_w/u_* between 1.4 and 1.6 on the upwind side of the Sotra Bridge (truss girder), which is consistent with the
 229 measurements conducted on the upwind side of the deck for the two wind sectors considered.

230 The ratio σ_w/σ_u estimated on the upwind side of the bridge is slightly above 0.6, in agreement with Kristensen and
 231 Jensen [2], which is larger than the value $\sigma_w/\sigma_u \approx 0.5$, usually found for a flat terrain [38]. On the other hand, only
 232 small differences are found for I_u and σ_v/σ_u between the downwind and upwind sides of the bridge deck, indicating
 233 that the horizontal components are not significantly affected by flow distortion from the girder. The unusually large ratio
 234 $\sigma_v/\sigma_u \approx 1$ obtained for a wind from south-southwest may, therefore, be attributed to terrain-induced flow distortion.
 235 For a wind from north-northeast, a more common value $\sigma_v/\sigma_u \approx 0.8$ is found, although it is still larger than for the
 236 Sotra Bridge experiment [2], which was slightly lower than 0.7. The considerable scatter obtained for σ_v/u_* and σ_u/u_* ,

237 for both wind directions, may also be attributed to local terrain effects rather than the influence of the bridge structure.
 238 Since Table 3 shows that the presence of the deck does not clearly affect I_u , the larger values of σ_u/u_* on the downwind
 239 side of the deck are likely caused by an underestimation of u_* due to flow distortion by the girder.

240 3.3. One-point velocity spectra

241 Figures 4 and 5 display the one-point auto and cross spectra normalized by the variance (or covariance) of the
 242 velocity estimated on the upwind side of the deck and expressed as a function of the reduced frequency f_r , for a flow
 243 from south-southwest and north-northeast, respectively. For the sake of clarity, only the PSD estimates from the sonic
 244 anemometers on H18W and H18E are displayed and superimposed to a semi-empirical velocity spectra model, shown
 245 as a black solid line. For the two horizontal velocity components and the real part of the cross-spectrum S_{uw} , the
 246 Kaimal spectral model [39] is chosen, whereas the Busch-Panofsky spectrum [40] is preferred for the vertical velocity
 247 component. In the field of micrometeorology, where these semi-empirical models have been defined, the spectra are
 248 generally normalized using the square of the friction velocity. In wind engineering, the variance of the velocity is
 249 traditionally used as a scaling parameter and is, therefore, used in the present case.

250 Both figures show that for $0.1 < f_r < 1$, the downwind vertical velocity spectra has a nearly constant value which is
 251 considerably lower than the spectral peak of both the reference semi-empirical spectra as well as the upwind spectra.
 252 Such a behaviour was previously observed by Hay [3] and demonstrates the influence of the bridge deck on the vertical
 253 wind velocity component. On the other hand, the two horizontal components show only minor differences between the

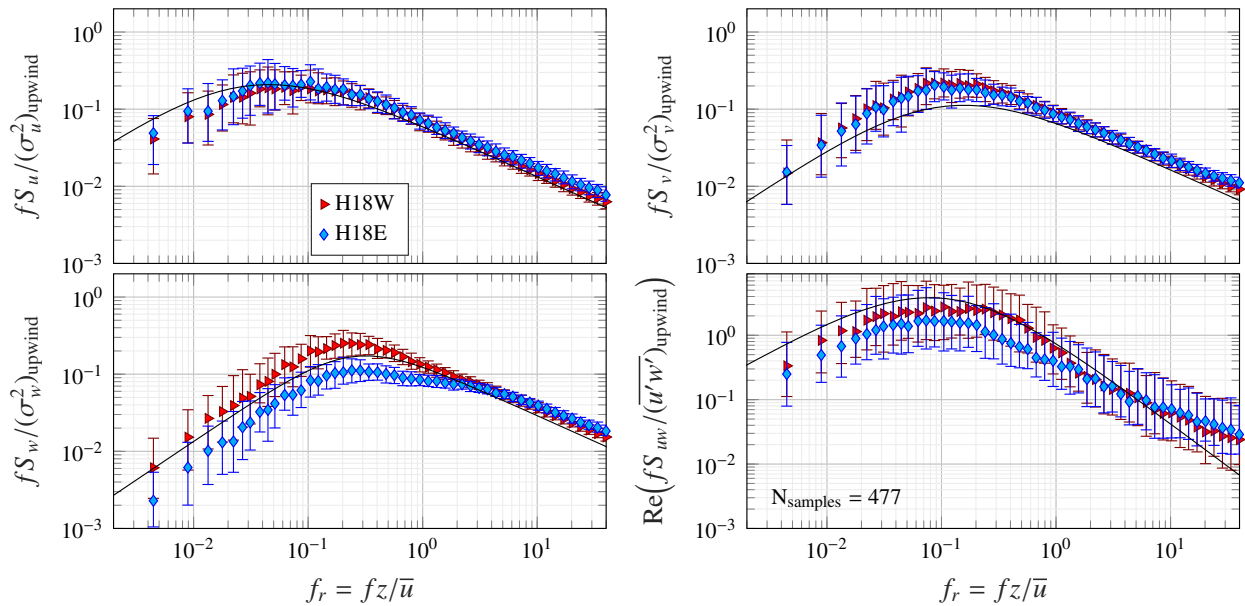


Figure 4: One-point auto and cross-spectral density estimates from the two sonic anemometers located at mid-span for a flow from south-southwest, near-neutral conditions and $\bar{u} > 6 \text{ m s}^{-1}$ at the deck height (415 samples). The error bar represents the interquartile range and the black solid lines the Kaimal spectral model (S_u , S_v spectra and cross-spectrum) and Busch-Panofsky spectrum (S_w spectrum).

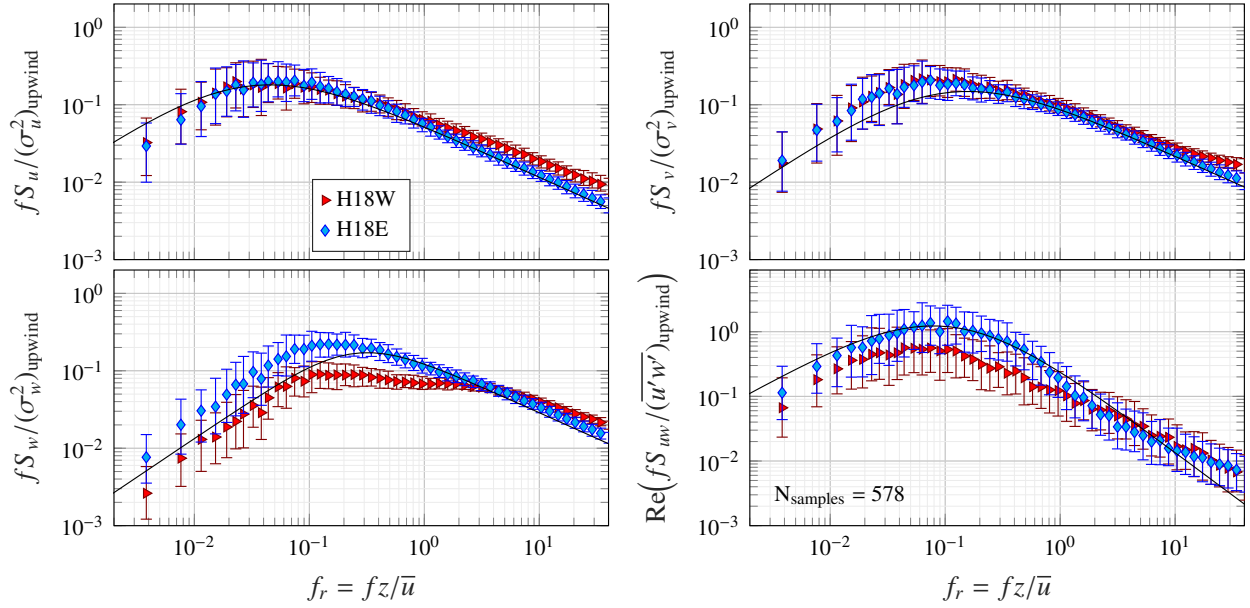


Figure 5: Same as in Figure 4 but for a wind from north-northeast (436 samples).

254 upwind or downwind side of the girder. Note that for a flow from north-northeast, the S_u spectrum on the downwind
 255 side shows values that are slightly larger than on the upwind side for $f_r > 1$, which is also observed for the flow from
 256 south-southwest, but to a lower degree. For a turbulent flow past a flat plate, Hunt and Graham [41] predicted an
 257 increase of the variance of the horizontal component normal to the plate and a decrease of the variance of the vertical
 258 component downwind of the leading edge. While the latter aspect is clearly observed in tables 2 and 3, the increased
 259 turbulence for the along-wind component is only visible in the high-frequency range of the PSD estimates, as shown in
 260 figs. 4 and 5 and has no clear consequences on the integrated turbulence characteristics.

261 For both wind sectors, the co-spectrum estimates from the downwind side of the deck are below those from the
 262 upwind side at $f_r < 1$, i.e. at the same reduced frequency as for the S_w spectrum, which can be attributed to the
 263 distortion of the flow by the deck. Velocity records from both sides of the deck show, however, discrepancies with the
 264 theoretical slope in $-7/3$ at $f_r > 3$, implying that the co-spectrum may, in addition, be influenced by the topography
 265 upstream of the deck.

266 3.4. Spectral ratios

267 The ratio of the PSD estimates of the vertical wind component over the along-wind component are ensemble-
 268 averaged and displayed in fig. 6 for a flow from south-southwest and in fig. 7 for a flow from the north-northeast. As
 269 predicted by the theory of local isotropy [42], S_w/S_u should reach a value of 1.33 in the inertial subrange, whereas
 270 a lower value is expected if the flow is distorted by the bridge deck. On the Sotra bridge (truss girder), Jensen and
 271 Hjort-Hansen [1] obtained a ratio S_w/S_u converging adequately toward 1.33 at $f_r > 2$ using sonic anemometers

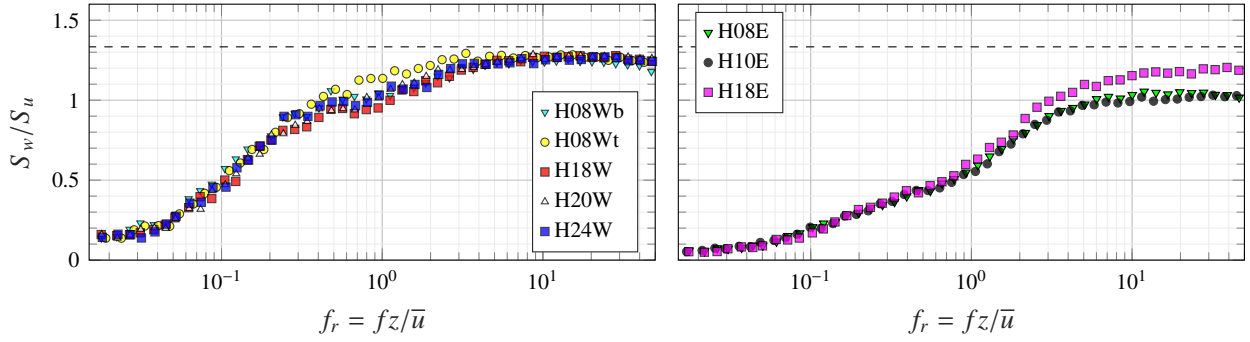


Figure 6: Ratio of the PSD estimates of the vertical wind component over the along-wind component for a flow from south-southwest, near-neutral conditions and $\bar{u} > 6 \text{ m s}^{-1}$ at the deck height (415 samples). The dashed line shows the theoretical ratio of 1.33.

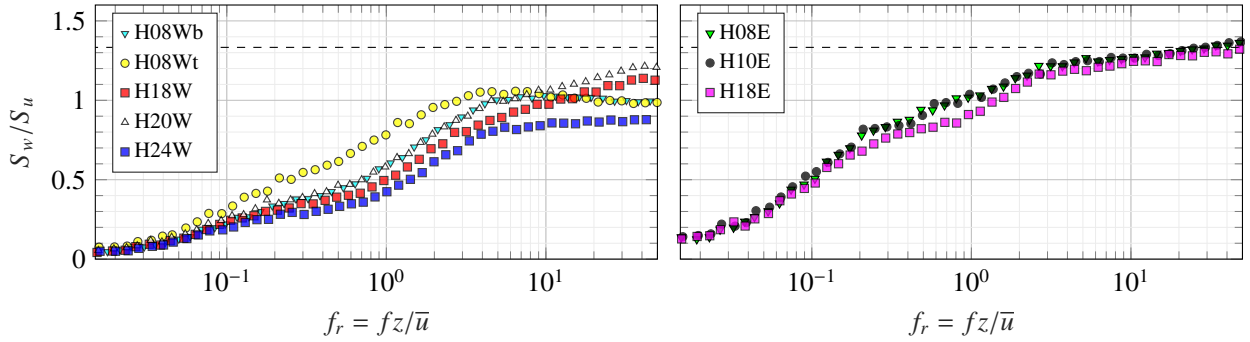


Figure 7: Same as in Figure 6 but for a wind from north-northeast (433 samples).

272 mounted 3 m on the upwind side of the deck, i.e. at a height of 60 m above the sea level, indicating undistorted flow
 273 conditions.

274 Figures 6 and 7 show that the ratio S_w/S_u obtained using the anemometers located on the downwind side of the
 275 bridge is significantly lower than upwind over the entire range of reduced frequencies. If the anemometer data from the
 276 upwind side are used, the ratio S_w/S_u converges toward a value ranging from 1.25 to 1.30 at $f_r > 5$, indicating that for
 277 a flow from south-southwest, the departure from the local isotropy may be due to a minor flow distortion on the upwind
 278 side of the deck, maybe due to the non-zero mean incidence angle. Note that the left panel of fig. 6 suggests that the
 279 flow recorded by the sonic anemometer mounted on H08Wb (6 m above the deck) on the upwind side may be affected,
 280 to a limited extent, by the presence of the deck at $0.6 < f_r < 2$, contrary to the sensor on H08Wt (10 m above the deck)
 281 which does not indicate any influence from the bridge deck when located upwind.

282 Figure 7 shows clearly that flow distortion is not uniform along the girder, as it is seen for flow from north-northeast,
 283 that the anemometer mounted on the southern part of the bridge records the strongest distortion with a ratio $S_w/S_u \approx 0.8$
 284 at $f_r \approx 10$, which for $z = 60 \text{ m}$ and $\bar{u} = 10 \text{ m s}^{-1}$ corresponds to $f = 1.7 \text{ Hz}$. Near $f_r \approx 1$, which for $z = 60 \text{ m}$ and
 285 $\bar{u} = 10 \text{ m s}^{-1}$ corresponds to the first eigenfrequencies of the bridge, the ratio S_w/S_u is also twice as low on the
 286 downstream side than on the upwind side, reinforcing the idea that the resonant buffeting response is underestimated

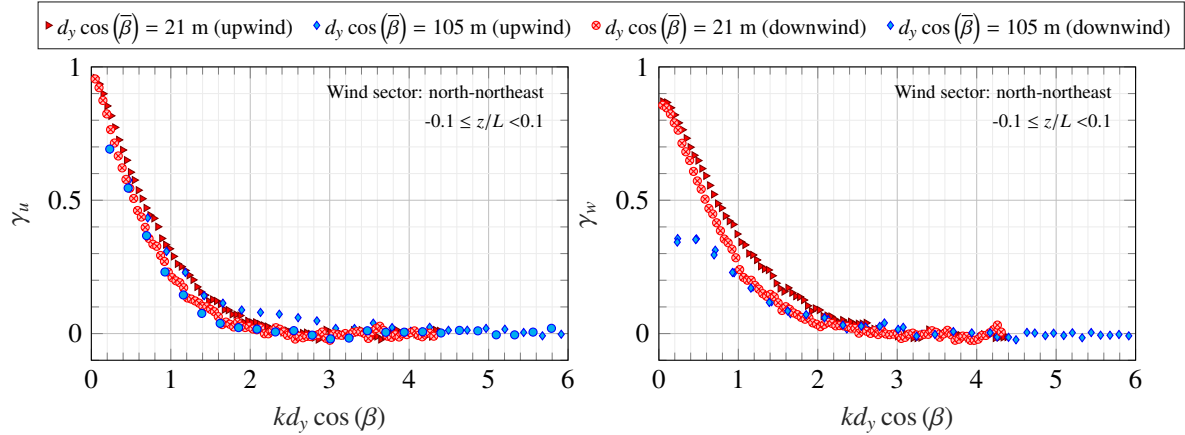


Figure 8: Along-span co-coherence estimates of the along-wind (left) and vertical (right) velocity components, for a flow from north-northeast, recorded at the upwind and downwind side of the bridge deck (444 samples).

287 if velocity records are gathered on the downstream side only. For a flow from south-southwest (fig. 6), the three
 288 anemometers located on the East side of the bridge show a similar level of flow distortion, except at $f_r > 4$ where the
 289 ratio S_w/S_u is smaller on the northern side of the bridge. The non-uniformity of the flow distortion along the span may
 290 be due to the large yaw angles recorded, such that the anemometers installed furthest from the initial separation point
 291 are located in a more developed turbulent layer. Another contributing factor may also be the asymmetric layout of the
 292 bridge girder with respect to its midspan, associated with the 7.5 m altitude difference between the north and south end.

293 3.5. Wind co-coherence

294 The ensemble-averaged along-span wind co-coherence for the u and w components is estimated on both the upwind
 295 and downwind side of the bridge. The goal is to establish how the coherence is affected by the presence of the girder.
 296 Figures 8 and 9 show such co-coherence estimates, which are evaluated using the same along-span separation lengths
 297 for a flow from north-northeast and south-southwest, respectively. Both wind sectors show that the deck is responsible
 298 for a slight decrease of the co-coherence on the downstream side, especially at low spatial separations. Nevertheless,
 299 this effect is relatively small and is only detectable in the present case because a large amount of samples is used, which
 300 allows an efficient smoothing of the coherence estimates.

301 An equally important challenge is the proper modelling of the co-coherence, as the right panels of Figures 8
 302 and 9 show that the Davenport model cannot capture efficiently γ_w at large lateral separations since γ_w is substantially
 303 lower than unity as the frequency approaches zero. Increasing discrepancies from the Davenport model are expected
 304 at $kd_y \cos(\beta) < 1$, which for a mean wind speed of 15 m s^{-1} and a crosswind separation of 20 m, corresponds to
 305 frequencies below 0.12 Hz. The latter frequency range coincides with the lowest vibrations modes of suspension
 306 bridges with a main span of 1 km or more, calling for an improved modelling of the co-coherence for the wind-resistant
 307 design of such structures.

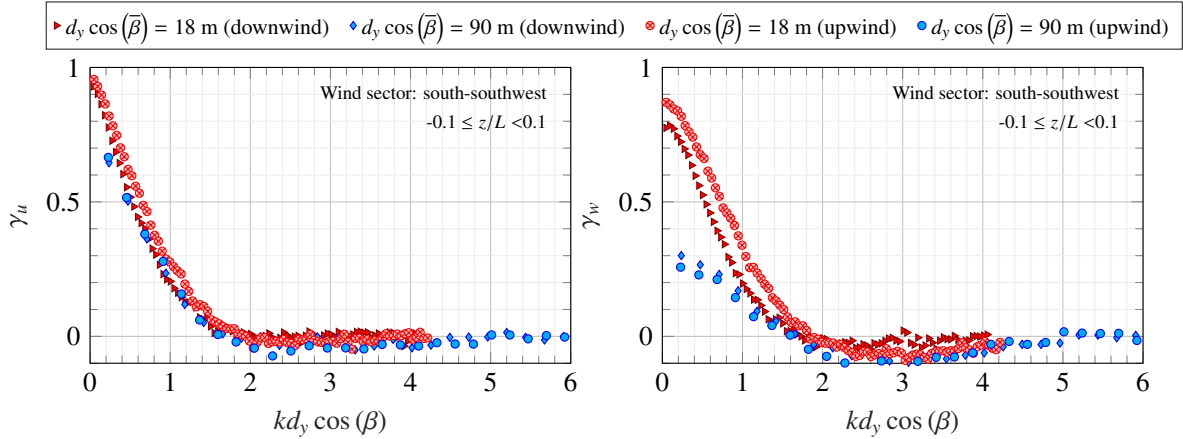


Figure 9: Same as in Figure 6 but for a wind from south-south-east (313 samples).

3.6. Influence of the sensor height on turbulence characterization

For a north-northeastern flow, the results presented in section 3 indicate that on the downstream side of the girder, even the sonic anemometer mounted 10 m above the deck (H08Wt) is affected by bridge-induced flow distortion. Figure 10 compares the normalized PSD estimates of the vertical wind velocity component on hanger 8, on both sides of the deck. For a flow from north-northeast (left panel of fig. 10), the two anemometers on the downwind side are those located at the height of 10 m (H08Wt) and 6 m (H08Wb) above the road, respectively. Their records show a reduced flow distortion at $f_r > 3$ only, which for $\bar{u} = 10 \text{ m s}^{-1}$ and $z = 60 \text{ m}$ corresponds to $f = 0.5 \text{ Hz}$, i.e. above the lowest eigenfrequencies of the Lysefjord bridge. At lower frequencies, the PSD estimates on H08Wt and H08Wb show significant discrepancies with the one estimated from H08E, assumed representative of undisturbed flow conditions.

A viable strategy to reduce deck-induced flow distortion is, therefore, to use anemometers on both sides of the girder, at a height corresponding to several deck heights. Flow distortion effects may also be expected in the measurement signal if the anemometers are installed on horizontal booms at the deck height. This was for example done by Xu and Zhu [8], who used 9 m-long booms mounted perpendicularly to a 41 m-wide deck. Using their fitted spectral model, the computed ratio S_w/S_u converges toward 0.7 in the inertial subrange, compared to 1.33 following local isotropy. The results displayed in section 3 corroborate also those from Hay [3], which showed that mounting a sonic anemometer at the centre of a deck (with a height $H = 3.2 \text{ m}$ and width $B = 31 \text{ m}$), even at a height of several meters above the road, should be avoided as flow distortion from every direction can be expected.

4. Wind-induced response of the Lysefjord bridge

4.1. Influence of model updating using improved data on the computed bridge response

The turbulence characteristics displayed in section 3 show that the underestimation of the vertical bridge response observed in Cheynet et al. [28] may be explained by the combination of girder-induced flow distortion and an incomplete

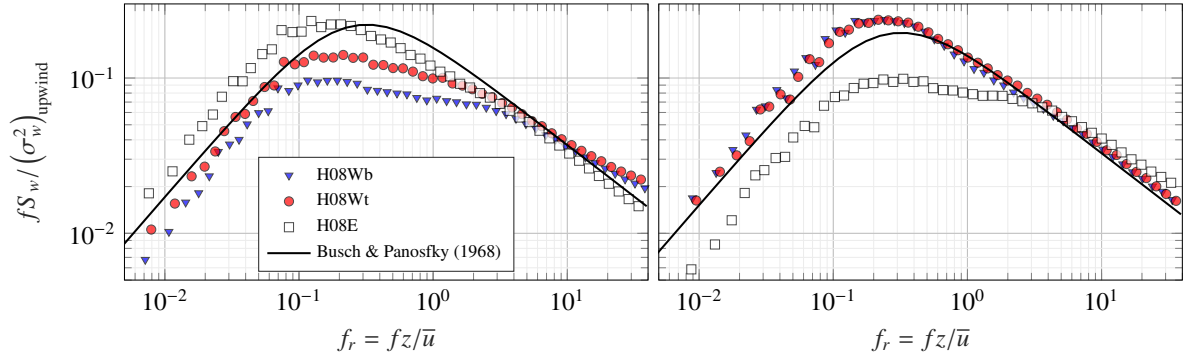


Figure 10: Vertical velocity spectra estimated on hangers 08 for a flow from north-northeast (left, 436 samples) and south-southwest (right, 415 samples).

329 anemometer calibration. The increased number of wind sensors and improved data post-processing allow, therefore, the
 330 modelling of an appropriate site-specific spectral model, summarized in fig. 11. In this figure, the characteristics of both
 331 the one-point and two-point spectra are summarized for a flow from north-northeast. The left and middle panel show the
 332 estimated and fitted co-coherence of the w component on the upwind side or downwind side of the deck, respectively.
 333 We recall that the west side of the deck is instrumented with more anemometers than the east side, which explains why
 334 the coherence on the downstream side is displayed for a larger variety of spatial separation than upwind. Finally, the
 335 right panel of fig. 11 corresponds to the estimated and fitted one-point velocity spectrum S_w at mid-span on both the
 336 upwind side and the downstream side of the girder. Note that the difference between the normalized PSD estimates for
 337 the downwind side in fig. 10 and fig. 11 are simply due to the fact that the latter figure shows the normalized spectra
 338 “as seen” by each sonic anemometer, whereas the former figure shows the spectra normalized by the variance of the
 339 “undisturbed” vertical velocity on the upwind side. The co-coherence is modelled using a least-square fit of eq. (15)
 340 to the full-scale co-coherence estimates. A similar procedure is done for the velocity spectrum S_w using eq. (12).
 341 Both eqs. (12) and (15) provide an excellent fit of the co-coherence and vertical velocity spectrum, respectively. The
 342 corresponding parameters for both wind sectors studied are summarized in Table 4, although only the case of a flow
 343 from north-northeast is considered in the following to study the buffeting response of the bridge.

344 The variance of the vertical acceleration and displacement response of the Lysefjord bridge is computed in the
 345 frequency domain using the wind load parameters displayed in fig. 11 for different mean wind speeds and in the case of
 346 a flow from north-northeast. This way, the influence of sensor position (upwind or downwind) on the computed bridge
 347 response is directly visualized. The computational responses are compared to full-scale measurements in fig. 12, which
 348 correspond to the 30 min acceleration records collected from July 2017 to May 2018.

349 Figure 12 suggests that the site-specific spectral model designed using the wind measurements on the upwind side
 350 of the deck leads to slightly conservative estimates for both the acceleration and displacement response. If the wind
 351 data on the downwind side are used, the computed acceleration response of the bridge agrees well with the measured
 352 one but underestimates the real one if the displacement response is considered. These results infer that the use of an

Table 4: Coefficients of the co-coherence (c_1, c_2, c_3) and one-point spectrum model (a_1, b_1, a_2, b_2) of the vertical wind velocity component, fitted in the least-square sense on the upwind and downwind side of the deck, for the two main wind direction recorded on the Lysefjord bridge.

Wind Direction	girder side	Co-coherence			One-point spectrum			
		c_1	c_2	c_3	a_1	b_1	a_2	b_2
North-northeast	Upwind	5.3	0.009	4.0	0.01	0.32	3.31	28.6
	Downwind	6.9	0.008	4.0	3.45	6.81	0.03	0.14
South-Southwest	Upwind	3.9	0.013	4.8	≈ 0	-	2.33	15
	Downwind	5.3	0.013	5.3	2.29	4.31	0.03	0.13

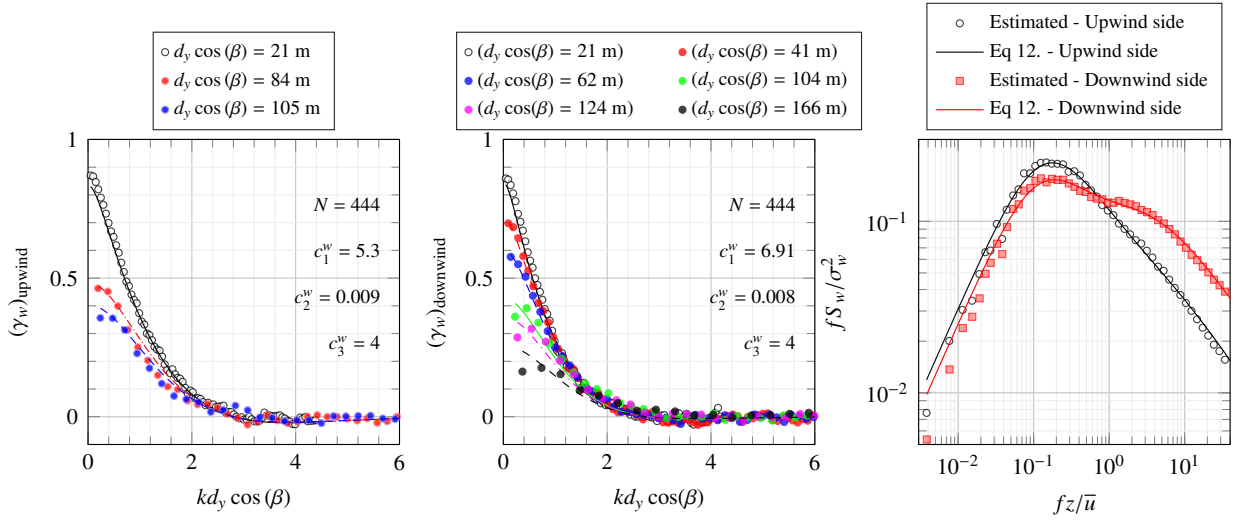


Figure 11: Estimated (scatter plot) and modelled (solid lines) co-coherence estimate (left panel) and one-point PSD estimate (right panel) of the vertical wind component for a flow from north-northeast, using velocity records from July 2017 to May 2018.

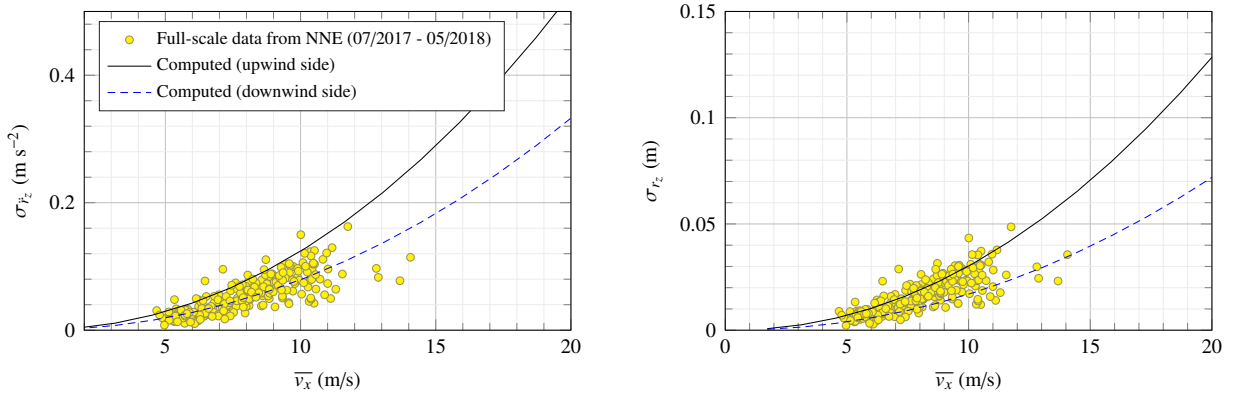


Figure 12: Computed and estimated standard deviation of the vertical bridge acceleration (left) and displacement(right) responses at mid-span using the data recorded from July 2017 to May 2018 for a flow from north-northeast.

353 aerodynamic admittance equal to unity at every frequency may not be appropriate for the study of the wind-induced
354 bridge acceleration response. Note that the displacement response has been high-pass filtered to remove the spurious
355 low-frequency component, which comes from the limited performances of the accelerometers at low frequencies. The
356 filter applied is a 5th order Butterworth filter with a cut-off frequency at 0.05 Hz.

357 4.2. Improved wind load model based on a modified cross-sectional admittance function

358 The strip theory assumes, in its basic form, that the wind field across the bridge is not significantly affected by the
359 presence of the deck so that the span-wise coherence of wind forces is equal to that of the undisturbed turbulence. An
360 extended model includes a cross-sectional admittance function, accounting for turbulence “averaging” across the bridge
361 deck as a function of the reduced frequency, $K = fB/\bar{u}$. In Larose [43], the significance of the turbulence integral
362 length scale relative to the deck width L_w/B on the lift force characteristics was demonstrated, using the cross-sectional
363 admittance function as well as the span-wise lift coherence. The latter was observed to be higher than the coherence of
364 the vertical turbulence, in line with the findings in Jakobsen [44], Larose et al. [45], Matsuda et al. [46].

365 The discussion on flow distortion in section 3 indicates a non-negligible influence of the structure on the oncoming
366 flow. In the following, the comparison between the computed and the recorded vertical bridge response is utilized to
367 study the cross-sectional admittance function in full-scale. The computed response is based on the assumption that
368 the horizontal wind velocity components have a negligible influence on the vertical buffeting response, and that the
369 span-wise coherence of the vertical turbulence, available from the measurements, is representative of the coherence of
370 the lift-force.

371 In full-scale studies, the approximation of a cross-sectional admittance function set equal to 1 for all frequencies
372 ($\chi_w \approx 1$) is commonly adopted. If the bridge displacement response is considered and if its most significant eigenfre-
373 quencies are well below 1 Hz, the approximation $\chi_w \approx 1$ is generally found acceptable. However, if the acceleration
374 response is used, the approximation $\chi_w \approx 1$ may no longer be valid, which appears to be the case of the Lysefjord
375 bridge. This is shown in fig. 13, where the acceleration and displacement spectra of the Lysefjord bridge vertical
376 response is estimated at mid-span using a 1-hour record duration on 21-11-2017 from 23:00, with a stationary mean
377 wind speed of 10 m s^{-1} and a flow from north-northeast. It is clearly seen that the use of $\chi_w \approx 1$ hampers the proper
378 decay of the acceleration response spectra with increased frequency of vibration, and thereby the overall acceleration
379 response is overestimated.

380 The choice of using a simple cross-sectional aerodynamic admittance function for the Lysefjord bridge is not
381 straightforward as the deck is somewhat bluff and, therefore, the Liepmann approximation of the Sears function [47] is
382 not necessarily suitable. For a closed-box girder with a ratio $H/B > 5$ and $0.2 < L_w/B < 2$, Larose [43] proposed an
383 empirical model that is an explicit function of both K and L_w/B . In fig. 13, $L_w/B \approx 4$ and $H/B = 4.5$, which is beyond
384 the scope of application for the model proposed by Larose [43]. If the latter model is used, the acceleration response
385 is underestimated. A simpler, but still suitable, cross-sectional admittance function for the Lysefjord bridge can be
386 defined as a second-order low-pass filter, independent of L_w/B , with a cut-off frequency at $K \approx 0.45$,

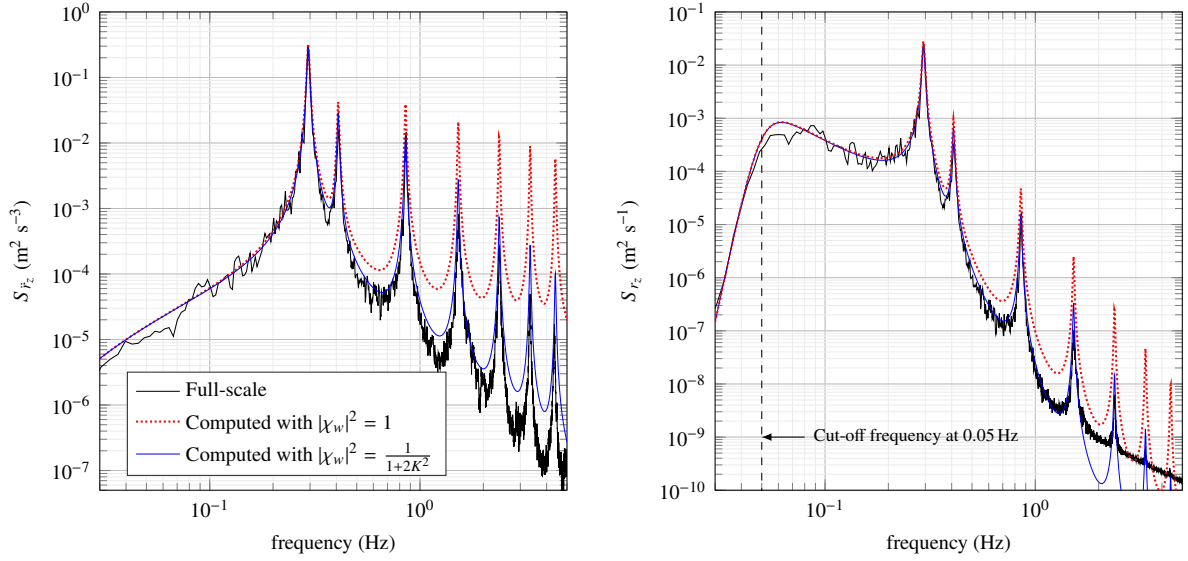


Figure 13: Full-scale 1-h acceleration (left panel) and displacement (right panel) spectrum of the Lysefjord bridge on 21-11-2017 superposed to the computed ones, which have been obtained using the spectral velocity model displayed in fig. 11 (upwind side) and different cross-sectional aerodynamic admittance functions.

$$|\chi_w(K)|^2 = \frac{1}{1 + aK^2} \quad (17)$$

387 where $a = 2$ is a parameter estimated in the least-square sense. The use of eq. (17) as a cross-sectional admittance
 388 function leads to an excellent agreement between the computed and full-scale acceleration spectra in fig. 13. As
 389 expected, the use of eq. (17) as a cross-sectional admittance function has a much smaller influence on the computed
 390 bridge displacement response than on the acceleration response. Although it might be a coincidence, eq. (17) with
 391 $a = 2$ is identical to the expression proposed by Hansen et al. [48] in the design basis of the Hardanger Bridge, which
 392 was modelled with a hexagonal closed box-girder with a ratio $B/H = 5.5$.

393 Even if eq. (17) is established using only 1 h of high-quality data, fig. 14 demonstrates that it greatly improves the
 394 agreement between the computed and estimated bridge response for the eleven months of acceleration record from July
 395 2017 to May 2018. In this figure, the acceleration and displacement response of the bridge is computed using the same
 396 spectral and coherence models (fig. 11), established on the upwind side of the girder. Note that the buffeting theory
 397 predicts that the turbulence intensity and the yaw angle are major sources of variability of the buffeting response of a
 398 wind-sensitive structure. Therefore, these have been accounted for in each sample considered in fig. 14. Other sources
 399 of discrepancies, such as the variation of the bridge deck aerodynamic coefficients with the yaw angle [49], the limited
 400 validity of the quasi-steady theory as well as the contribution of the bridge towers and main cables to aerodynamic
 401 loading [50] are not included herein for the sake of simplicity. Finally, it should be noted that the results shown in
 402 fig. 14 are consistent with those displayed in fig. 12 and fig. 13, where the use of eq. (17) as a cross-sectional admittance

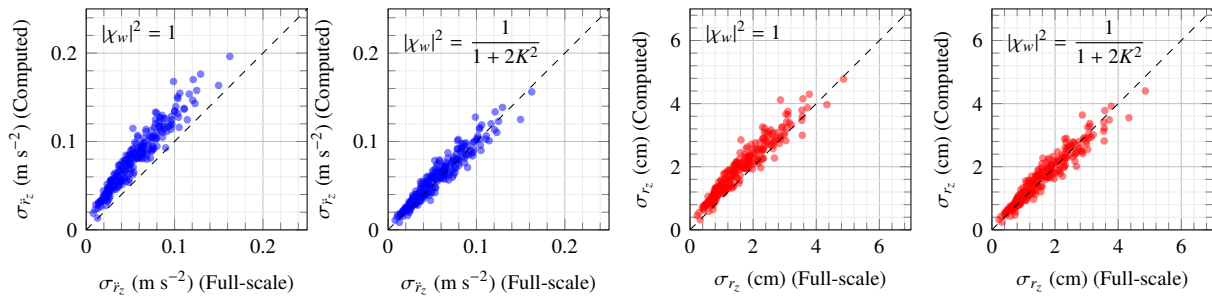


Figure 14: Standard deviation of the vertical acceleration and displacement response of the bridge at mid-span using full-scale data from July 2017 to May 2018 (horizontal axis) and a computational model (vertical axis) relying on the spectral velocity model recorded on the upwind side and two different cross-sectional admittance functions χ_w .

403 function has a much more visible effect on the acceleration response than on the displacement response.

404 5. Conclusions

405 Eleven months of wind velocity data collected by sonic anemometers mounted above the deck of a suspension
 406 bridge crossing the inlet of a fjord in south-western Norway have been studied. The complexity of the recorded flow is
 407 augmented by distortions caused by the bridge girder and the mountainous surroundings, as well as imperfections in the
 408 anemometer setup. Using an improved and extended bridge instrumentation as well as a rigorous data post-processing
 409 focusing on high-quality data only, the different sources of flow distortion have been identified, leading to the following
 410 findings:

- 411 • The vertical velocity component w recorded on the downstream side of the deck is underestimated because
 412 of deck-induced flow distortion. On the other hand, the two horizontal wind components u and v are much
 413 more affected by the terrain than by the girder. Consequently, the turbulence characteristics established for both
 414 a wind from south-southwest and north-northeast can greatly deviate from the case of flat and homogeneous
 415 terrain. In particular, the ratio σ_w/σ_u might be as high as 0.7 in a narrow fjord whereas in flat and homogeneous
 416 terrain $\sigma_w/\sigma_u \approx 0.5$. For the two main wind directions considered, the flow is not affected the same way by the
 417 topography, which reinforces the idea that turbulence characteristics observed on a bridge crossing a fjord or a
 418 canyon should be studied separately for different sectors.
- 419 • For a hexagonal girder with a width to height ratio $B/H \approx 4.5$, mounting a sonic anemometer at a height
 420 equal to $3.6H$ above the deck instead of $2.2H$ shows only minor improvements in flow distortion mitigation
 421 if located downwind. To study turbulence characteristics from a long-span bridge, it is thus advised to mount
 422 sonic anemometers on both sides of the girder. Such an installation is particularly important in a mountainous
 423 area where the characterization of the wind conditions needs to be conducted after separation of the records in

424 different wind sectors, where some of the anemometers will inevitably be located on the downstream side of the
425 deck.

- 426 • If the wind velocity measurements are conducted on the downstream side of the deck, the wind load is substantially
427 underestimated, compared to measurements on the upstream side, which are affected to a lower degree by the
428 flow disturbance of the bridge deck. The bridge response estimation is, however, observed to be sensitive to
429 the bridge cross-sectional admittance applied. Assuming a simple admittance function equal to unity at every
430 frequency will result in an overestimation of response when used with wind data measured upstream, but may
431 lead to a reasonable agreement between computed and recorded response when used with wind data measured
432 downstream. However, it is shown herein, that modelling the admittance function as a simple second order filter
433 will lead to a significantly improved agreement between the computed and observed full-scale bridge response,
434 when used in combination with wind load information collected on the upwind side of the deck

435 **Acknowledgements**

436 The support of the Norwegian Public Roads Administration is gratefully acknowledged, as well as their assistance
437 during the installation and maintenance of the monitoring system.

438 **References**

439 **References**

- 440 [1] Jensen N, Hjort-Hansen E. Dynamic excitation of structures by wind-turbulence and response measurements at the Sotra Bridge. Tech. Rep.
441 Report No. STF71 A.; SINTEF; 1977.
- 442 [2] Kristensen L, Jensen NO. Lateral coherence in isotropic turbulence and in the natural wind. *Boundary-Layer Meteorology* 1979;17(3):353–73.
- 443 [3] Hay JS. Analyses of wind and response data from the Wye and Erskine Bridges and comparison with theory. *Journal of wind engineering and*
444 *industrial aerodynamics* 1984;17(1):31–49.
- 445 [4] Bietry J, Delaunay D, Conti E. Comparison of full-scale measurement and computation of wind effects on a cable-stayed bridge. *Journal of*
446 *wind engineering and industrial aerodynamics* 1995;57(2):225–35.
- 447 [5] Toriumi R, Katsuchi H, Furuya N. A study on spatial correlation of natural wind. *Journal of Wind Engineering and Industrial Aerodynamics*
448 2000;87(2):203–16.
- 449 [6] Miyata T, Yamada H, Katsuchi H, Kitagawa M. Full-scale measurement of Akashi-Kaikyō Bridge during typhoon. *Journal of wind engineering*
450 *and industrial aerodynamics* 2002;90(12):1517–27.
- 451 [7] Macdonald JH. Evaluation of buffeting predictions of a cable-stayed bridge from full-scale measurements. *Journal of wind engineering and*
452 *industrial aerodynamics* 2003;91(12):1465–83.
- 453 [8] Xu Y, Zhu L. Buffeting response of long-span cable-supported bridges under skew winds. Part 2: case study. *Journal of Sound and Vibration*
454 2005;281(3):675–97.
- 455 [9] Hay JS. The wind-induced response of the Erskine Bridge; chap. 6. ICE publishing; 1981, p. 81–90.
- 456 [10] Frandsen J. Simultaneous pressures and accelerations measured full-scale on the Great Belt East suspension bridge. *Journal of Wind*
457 *Engineering and Industrial Aerodynamics* 2001;89(1):95 – 129.

- 458 [11] Snæbjörnsson JT, Jakobsen JB, Cheynet E, Wang J. Full-scale monitoring of wind and suspension bridge response. *IOP Conference Series: Materials Science and Engineering* 2017;276(1):012007.
- 459
- 460 [12] Nakai T, Van der Molen M, Gash J, Kodama Y. Correction of sonic anemometer angle of attack errors. *Agricultural and Forest Meteorology* 2006;136(1-2):19–30.
- 461
- 462 [13] Nakai T, Shimoyama K. Ultrasonic anemometer angle of attack errors under turbulent conditions. *Agricultural and forest meteorology* 2012;162:14–26.
- 463
- 464 [14] Vickers D, Mahrt L. Quality control and flux sampling problems for tower and aircraft data. *Journal of Atmospheric and Oceanic Technology* 1997;14(3):512–26.
- 465
- 466 [15] Stiperski I, Rotach MW. On the measurement of turbulence over complex mountainous terrain. *Boundary-Layer Meteorology* 2016;159(1):97–121.
- 467
- 468 [16] Paw U KT, Baldocchi DD, Meyers TP, Wilson KB. Correction of eddy-covariance measurements incorporating both advective effects and density fluxes. *Boundary-Layer Meteorology* 2000;97(3):487–511.
- 469
- 470 [17] Wilczak JM, Oncley SP, Stage SA. Sonic anemometer tilt correction algorithms. *Bound-Layer Meteorol* 2001;99(1):127–50.
- 471 [18] McMillen RT. An eddy correlation technique with extended applicability to non-simple terrain. *Boundary-Layer Meteorology* 1988;43(3):231–45.
- 472
- 473 [19] Klipp C. Turbulent friction velocity calculated from the Reynolds stress tensor. *Journal of the Atmospheric Sciences* 2018;75(4):1029–43.
- 474 [20] Shinozuka M, Deodatis G. Simulation of stochastic processes by spectral representation. *Applied Mechanics Reviews* 1991;44(4):191–204.
- 475 [21] Weber R. Remarks on the definition and estimation of friction velocity. *Boundary-Layer Meteorol* 1999;93(2):197–209.
- 476 [22] Nieuwstadt FT. The turbulent structure of the stable, nocturnal boundary layer. *J Atmos Sci* 1984;41(14):2202–16.
- 477 [23] Sorbjan Z. On similarity in the atmospheric boundary layer. *Boundary-Layer Meteorol* 1986;34(4):377–97.
- 478 [24] Welch PD. The use of fast Fourier transform for the estimation of power spectra: A method based on time averaging over short, modified periodograms. *IEEE Trans Audio Electroacoustics* 1967;15:70–3.
- 479
- 480 [25] Davenport A. The buffeting of large superficial structures by atmospheric turbulence. *Annals of the New York Academy of Sciences* 1964;116(1):135–60.
- 481
- 482 [26] Scanlan R. The action of flexible bridges under wind, II: Buffeting theory. *Journal of Sound and vibration* 1978;60(2):201–11.
- 483 [27] Cheynet E. Wind-induced vibrations of a suspension bridge: A case study in full-scale. Ph.D. thesis; University of Stavanger, Norway; 2016.
- 484 [28] Cheynet E, Jakobsen JB, Snæbjörnsson J. Buffeting response of a suspension bridge in complex terrain. *Engineering Structures* 2016;128:474–87.
- 485
- 486 [29] Xie J, Tanaka H, Wardlaw R, Savage M. Buffeting analysis of long-span bridges to turbulent wind with yaw angle. *Journal of Wind Engineering and Industrial Aerodynamics* 1991;37(1):65 – 77.
- 487
- 488 [30] Saranyasoontorn K, Manuel L, Veers PS. A comparison of standard coherence models for inflow turbulence with estimates from field measurements. *J Sol Energy Eng* 2004;126(4):1069–82.
- 489
- 490 [31] Sigbjörnsson R, Hjorth-Hansen E. Along-wind response of suspension bridges with special reference to stiffening by horizontal cables. *Engineering Structures* 1981;3(1):27–37.
- 491
- 492 [32] Strømmen EN. *Structural Dynamics; chap. Eigenvalue Calculations of Continuous Systems*. Cham: Springer International Publishing. ISBN 978-3-319-01802-7; 2014, p. 89–159. doi:10.1007/978-3-319-01802-7_3.
- 493
- 494 [33] Magalhães F, Cunha A, Caetano E. Online automatic identification of the modal parameters of a long-span arch bridge. *Mechanical Systems and Signal Processing* 2009;23(2):316 –29. doi:10.1016/j.ymssp.2008.05.003.
- 495
- 496 [34] Davenport AG. The spectrum of horizontal gustiness near the ground in high winds. *Q J R Meteorol Soc* 1961;87(372):194–211. doi:10.1002/qj.49708737208.
- 497
- 498 [35] Harstveit K. Full-scale measurements of gust factors and turbulence intensity, and their relations in hilly terrain. *Journal of wind engineering and industrial aerodynamics* 1996;61(2-3):195–205.
- 499
- 500 [36] Cheynet E, Jakobsen JB, Snæbjörnsson J, Reuder J, Kumer V, Svardal B. Assessing the potential of a commercial pulsed lidar for wind

- 501 characterisation at a bridge site. *Journal of Wind Engineering and Industrial Aerodynamics* 2017;161:17–26.
- 502 [37] De Franceschi M, Zardi D, Tagliazucca M, Tampieri F. Analysis of second-order moments in surface layer turbulence in an Alpine valley.
503 *Quarterly Journal of the Royal Meteorological Society* 2009;135(644):1750–65.
- 504 [38] Solari G, Piccardo G. Probabilistic 3-D turbulence modeling for gust buffeting of structures. *Probabilistic Engineering Mechanics* 2001;16(1):73–
505 86.
- 506 [39] Kaimal JC, Wyngaard J, Izumi Y, Coté O. Spectral characteristics of surface-layer turbulence. *Quarterly Journal of the Royal Meteorological*
507 *Society* 1972;98(417):563–89.
- 508 [40] Busch NE, Panofsky HA. Recent spectra of atmospheric turbulence. *Quarterly Journal of the Royal Meteorological Society* 1968;94(400):132–
509 48.
- 510 [41] Hunt J, Graham J. Free-stream turbulence near plane boundaries. *Journal of Fluid Mechanics* 1978;84(2):209–35.
- 511 [42] Kolmogorov AN. The local structure of turbulence in incompressible viscous fluid for very large Reynolds numbers. In: *Dokl. Akad. Nauk*
512 *SSSR*; vol. 30. 1941, p. 299–303.
- 513 [43] Larose GL. The spatial distribution of unsteady loading due to gusts on bridge decks. *Journal of wind engineering and industrial aerodynamics*
514 2003;91(12-15):1431–43.
- 515 [44] Jakobsen JB. Span-wise structure of lift and overturning moment on a motionless bridge girder. *Journal of wind engineering and industrial*
516 *aerodynamics* 1997;69:795–805.
- 517 [45] Larose G, Tanaka H, Gimsing N, Dyrbye C. Direct measurements of buffeting wind forces on bridge decks. *Journal of Wind Engineering and*
518 *Industrial Aerodynamics* 1998;74:809–18.
- 519 [46] Matsuda K, Hikami Y, Fujiwara T, Moriyama A. Aerodynamic admittance and the strip theory for horizontal buffeting forces on a bridge deck.
520 *Journal of Wind Engineering and Industrial Aerodynamics* 1999;83(1-3):337–46.
- 521 [47] Liepmann H. On the application of statistical concepts to the buffeting problem. *Journal of the Aeronautical Sciences* 1952;19(12):793–800.
- 522 [48] Hansen S, Lollesgaard M, Rex S, Jakobsen J, Hjorth-Hansen E. The Hardanger bridge: Static and dynamic wind tunnel tests with a section
523 model. prepared for the Norwegian Public Roads Administration. Tech. Rep. Revision 1; Svend Ole Hansen ApS.; 2006.
- 524 [49] Zhu L, Xu Y, Zhang F, Xiang H. Tsing Ma bridge deck under skew winds—part I: Aerodynamic coefficients. *Journal of Wind Engineering*
525 *and Industrial Aerodynamics* 2002;90(7):781–805.
- 526 [50] Wang J, Cheynet E, Jakobsen JB, Snæbjörnsson J. Time-domain analysis of wind-induced response of a suspension bridge in comparison with
527 the full-scale measurements. In: *ASME 2017 36th International Conference on Ocean, Offshore and Arctic Engineering*. American Society of
528 *Mechanical Engineers*; 2017, p. V03BT02A032–.